Available online at www.sciencedirect.com
ScienceDirect
Journal of Nuclear Materials 358 (2006) 10–25
journal of nuclear materials
www.elsevier.com/locate/jnucmat

Formation of steady state size distribution of precipitates in alloys under cascade-producing irradiation

A.A. Turkin *, A.S. Bakai

National Science Center 'Kharkov Institute of Physics and Technology', 1 Akademicheskaya str., UA-61108 Kharkov, Ukraine

Received 12 December 2005; accepted 25 May 2006

Abstract

The effect of coherency loss on the development of precipitate size distribution under cascade-producing irradiation is considered. The nucleation of coherent precipitates, their growth followed by coherency loss and cascade-induced dissolution of large incoherent precipitates can occur simultaneously resulting in formation of a quasi-stationary size distribution of semicoherent precipitates. To describe this process we consider co-evolution of a mixed population of coherent, semicoherent and incoherent precipitates. Mathematically, the problem is formulated as a set of discrete rate equations of nucleation kinetics (the Master equation approach) which is also used for later stages of evolution. To solve the corresponding large set of equations (typically, more than 10^5 equations) an efficient numerical method is developed. The simulation results obtained for material parameters and irradiation conditions typical for nuclear reactors show that the coherency loss affects considerably evolution of the precipitate population. Under certain irradiation conditions, both in solution-annealed alloys and in aged ones, the mean precipitate size and the number density during prolonged irradiation tend to steady state values, whereas the size distribution function of large precipitates narrows. The width of the quasi-stationary size distribution is controlled by cascade parameters. It was found that the asymptotic quasi-stationary state of the precipitate population may depend on initial state of the alloy.

PACS: 61.80.Az; 61.82.Bg; 81.30.Mh

1. Introduction

Modern multicomponent alloys applied in nuclear industry contain precipitates of non-equilibrium phases and/or phases supersaturated with one of the components. During in-reactor service the alloy composition and phase microstructure evolve, resulting in change of mechanical properties and dimensional instability. Several examples presented below show that second phase precipitation plays a very important role in behavior of materials under irradiation.

It is frequently found that materials exhibit enhanced radiation resistance if second phase precipitates are coherent with the matrix, e. g. the swelling resistance of PE16 stainless steel [1] and other nickel-rich alloys [2,3] is attributed usually to the

* Corresponding author. Tel.: +380 57 335 6203; fax: +380 57 335 2683.
E-mail address: a.turkin@kipt.kharkov.ua (A.A. Turkin).

0022-3115/$ - see front matter © 2006 Elsevier B.V. All rights reserved.
doi:10.1016/j.jnucmat.2006.05.054

population of fine-grained precipitates of γ′-phase homogeneously distributed in the matrix.

Another example is the formation of a high number density of ultra-fine, nanometer-sized copper-rich precipitates in ferritic steels which is a major cause of steel hardening and embrittlement of reactor pressure vessels [4,5]. Much research attention has concentrated on the precipitation of copper in binary Fe–Cu model alloys under thermal ageing conditions. These studies have established that the copper-rich precipitates first form with a coherent bcc structure, while large overaged precipitates are fcc. The precipitate structures follow a complicated sequence of transformations from coherent into incoherent state, bcc → 9R → 3R → fcc, with increasing aging time [6,7]. The size at which the first transformation bcc → 9R takes place depends on the ambient temperature and is about 12 nm at 550 °C and 5 nm at room temperature [7]. A similar precipitation sequence has been observed in a Fe–1.5 wt%Cu alloy irradiated at 295 °C with 2.5 MeV electrons to a dose of 3.1×10^{23} m^{-2}. The maximum size of 9R precipitates found here was about 8 nm, larger precipitates (up to about 20 nm) appeared to have transformed wholly or partially to 3R or fcc [8]. This suggests that the main effect of electron irradiation was to enhance the diffusion of copper and, hence, to accelerate the precipitation kinetics. Under neutron and ion irradiation the precipitate evolution differs. The presence of small 9R precipitates was confirmed in a Fe–1.3 wt%Cu model alloy irradiated with neutrons to doses of 8.61×10^{-3} dpa and 6.3×10^{-2} dpa at a temperature of about 270 °C [9]. However, studies reported in [9], the earlier small-angle neutron scattering (SANS) and transmission electron microscopy data [10], as well as the recent atom probe tomography and SANS studies [11] have found that in both steels and model alloys, precipitate sizes are smaller (about 2–4 nm) and number densities are higher after neutron irradiation than for equivalent thermally-aged materials. The size decrease of Cu precipitates in an aged Fe–1.3 wt%Cu alloy was observed in the temperature range between room temperature and 550 °C after 300 keV Fe^+ ion irradiation at displacement rates of 10^{-3}–10^{-2} dpa/s to fluences of up to 30 dpa [12]. Copper precipitates were found to keep their shape but decrease in size under all irradiation conditions. According to [9,12], the lack of coarsening seen in precipitates under neutron and heavy-ion irradiation may be due to cascade-induced precipitate dissolution.

It is known that Zr–Nb alloys are usually fabricated with a dual α-Zr + β-Zr phase structure. Both phases are metastable under operating temperatures of thermal reactors (about 520–570 K). The hcp α-phase is supersaturated with Nb. Precipitation of β-Nb in the α-phase correlates with the improved corrosion resistance of the Zr–2.5Nb pressure tubes due to irradiation (see, for example [13] and papers cited there). The radiation-enhanced β-Nb precipitation in the form of needles, platelets or sword-shaped precipitates has been observed under electron [14] proton [15] and neutron [13,16–20] irradiation. In irradiated samples the average size of β-Nb precipitates is generally small, 5–40 nm in length. The density of precipitates is high and generally they are distributed uniformly within the α-Zr phase. We have not found in the literature any observations of large incoherent globular Nb precipitates or precipitates at grain boundaries in the α-Zr phase irradiated under reactor conditions, i.e. at temperatures below 600 K. In our opinion, this indicates that incoherent precipitates are unstable under irradiation and therefore cannot form. At the same time, stability of small platelet or needle-like precipitates under irradiation can be understood if we note that these precipitates are in a more coherent state with the α-Zr matrix [24]. In reality, β-Nb particles cannot be fully coherent with the α-matrix because of different crystal lattices. However, a large fraction of the interface of a needle-, platelet- or sword-shaped particle is coherent with the matrix, while the lattice misfit is accommodated at the incoherent fraction of the interface. This means that on the average the small β-Nb precipitates can be considered coherent (or semicoherent) with the matrix. *It seems that in alloys under certain irradiation conditions coherent precipitates cannot grow to large sizes because of coherency loss.*

In our previous publications we have described the combined effect of radiation-induced segregation and cascades mixing on the stability of coherent and incoherent precipitates in disordered substitutional alloys. The results of phase stability studies have been presented in the form of radiation-modified phase diagram [21–24]. This diagram contains a low temperature boundary for precipitate stability, the location of which depends on displacement rate and mixing efficiency of irradiation. We have found that stability criteria for coherent and incoherent precipitates differ. The low temperature boundary for stability of incoherent precipitates is located at higher temperatures than the corresponding

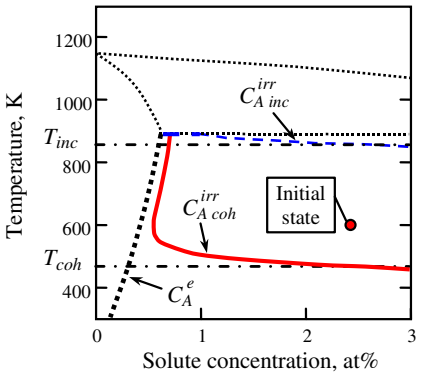

Fig. 1. Radiation-modified phase diagram of a model alloy calculated for cascade-producing irradiation without segregation effects [24] (material parameters are listed in Table 1). The equilibrium phase diagram of the Zr–Nb alloy is shown by dotted lines as a reference to real materials. The initial state of the alloy shown by the full circle corresponds to stable coherent precipitates and unstable incoherent precipitates. The equilibrium concentration of mobile monomers and radiation-modified solubilities (coherent and incoherent) are labeled by C_A^e, $C_{A\,coh}^{irr}$ and $C_{A\,inc}^{irr}$, correspondingly.

boundary for coherent precipitates, $T_{coh} < T_{inc}$ (see Fig. 1). The existence of two thresholds for stability of precipitates suggests that in alloys under irradiation at temperatures $T_{coh} < T < T_{inc}$ a quasi-stationary distribution of semicoherent precipitates may form [24]. The mechanism is connected with competition of (i) the nucleation and growth of coherent precipitates in a supersaturated solid solution and (ii) the cascade-induced dissolution of large precipitates that lose coherency upon reaching, during growth, some critical range of sizes. The supersaturation in the alloy can be created and maintained due to cascade-induced dissolution of incoherent precipitates present in the alloy prior to irradiation.

The aim of this paper is to investigate the effect of coherency loss on the development of precipitate size distribution under cascade-producing irradiation. In the next section we construct the precipitate growth rate as a function of a degree of coherency. Then, in order to describe the evolution of the mixed population of coherent, semicoherent and incoherent precipitates, we formulate the discrete Master equation approach, i.e. the set of kinetic equations for the entire population of solute clusters of all sizes together with mobile monomers and point defects (PD). The influence of coherency loss on the sink strength, point defect concentrations and growth rates of precipitates is taken into account self-consistently. To solve the set of kinetic equations we develop an efficient numerical method. Finally, using parameters typical for reactor materials, we demonstrate that under irradiation a quasi-stationary distribution of precipitates can form both in solution-annealed alloys and in aged ones.

2. The model

Consider a substitutional binary alloy A–B with concentrations of components C_A and C_B ($C_A + C_B = 1$, $C_B > C_A$, where C_A is the solute in the following). The concentrations are defined in terms of atomic fractions. The alloy may contain coherent and incoherent precipitates of an ordered phase, which is assumed to consist of pure component A. To keep the matter simple and to demonstrate the effect of coherency loss we neglect radiation-induced segregation and consider only cascade-induced dissolution as a mechanism of phase stability loss. All precipitates are approximated as spherical in shape. The rate of precipitate growth can be represented as a sum of two contributions, namely, the diffusion growth and the cascade-induced dissolution due to atomic mixing inside cascade regions

$$\frac{dR}{dt} = \left(\frac{dR}{dt}\right)_{dif} + \left(\frac{dR}{dt}\right)_{mix}, \tag{1}$$

where R is the precipitate radius. Using results of [22,24], one can show that in the absence of segregation effects the diffusion-controlled growth rate of coherent and incoherent precipitates is given by

$$\left(\frac{dR}{dt}\right)_{dif}^{\alpha} = \frac{D_A^{\alpha}}{R}(C_A - C_A^{R,\alpha}) \quad \alpha = \mathrm{coh}, \mathrm{inc}, \tag{2}$$

where superscripts coh and inc refer to coherent and incoherent precipitates, respectively; C_A is the average concentration of mobile solute monomers in the matrix. $C_A^{R,\alpha}$ is the thermal equilibrium concentration of solute monomers at the precipitate boundary given by the Gibbs–Thomson relation

$$C_A^{R,\alpha} = C_A^{e,\alpha} \exp\left(\frac{2\gamma_\alpha \omega}{R k_B T}\right), \tag{3}$$

where $C_A^{e,\alpha}$ is the solute monomer concentration at equilibrium with the bulk phase A and γ_α is the precipitate–matrix interphase energy. $C_A^{e,\alpha}$ and γ_α depends on interface type. Generally, the interphase energy of coherent precipitates is substantially less than that of incoherent precipitates [25]. The

coefficient of radiation-enhanced interdiffusion D_A^{α} depends on interface type [21]

$$D_A^{coh} = D_V(2C_V - C_V^e), \quad D_A^{inc} = \frac{2D_V(C_V - C_V^e)}{\ln(2C_V/C_V^e - 1)}, \tag{4}$$

where D_V is the vacancy diffusion coefficient, C_V is the average concentration of vacancies and C_V^e is the thermal equilibrium concentration of vacancies. Under irradiation the vacancy supersaturation $C_V/C_V^e \gg 1$, therefore, according to Eqs. (2) and (4), the diffusion growth rate of incoherent precipitates is less than the diffusion growth rate of coherent ones. The physical reason is that the boundary of the incoherent precipitate is a sink for PD and thermal equilibrium concentrations of PD are maintained at it. Therefore, near the incoherent precipitate concentrations of PD is less than near the coherent precipitate, hence the solute diffusion is retarded.

It is reasonable to assume that the rate of athermal cascade dissolution is the same for coherent and incoherent precipitates

$$\left(\frac{dR}{dt}\right)_{mix} = -\frac{D_{mix}}{R}, \tag{5}$$

where D_{mix} is the diffusion coefficient due to cascade mixing, which is proportional to the mixing efficiency d_{mix} and the generation rate of freely migrating PD K [23,24].

$$D_{mix} = d_{mix}K. \tag{6}$$

Now we will derive the growth rate of a semicoherent precipitate. To take into account the coherency loss we introduce the size dependent degree of coherency. The transformation from the coherent state into the incoherent one is assumed to occur gradually in a certain size interval. The degree of coherency for a precipitate containing n solute atoms we define by a step-like function

$$p = \begin{cases} 1, & \text{for } n \leqslant n_{coh} \\ \left[1 + \exp\left(\dfrac{n - n_{loss}}{\Delta n}\right)\right]^{-1}, & \text{for } n > n_{coh} \end{cases} \quad n = \frac{4\pi}{3\omega}R^3, \tag{7}$$

where n_{loss} is the size of the precipitate with $p = 0.5$, Δn is the width of the transformation region and ω is the atomic volume. Small precipitates (solute clusters) containing less than n_{coh} atoms are considered to be coherent with the matrix ($n_{coh} < n_{loss}$).

The growth rate of semicoherent precipitate is constructed as an interpolation between the growth rates of coherent and incoherent precipitates with the degree of coherency as a weighting factor

$$\frac{dR}{dt} = \left(\frac{dR}{dt}\right)_{dif}^{coh} p + \left(\frac{dR}{dt}\right)_{dif}^{inc}(1-p) + \left(\frac{dR}{dt}\right)_{mix}. \tag{8}$$

Our goal is to consider the evolution of the precipitate size distribution function which is defined as the time-dependent concentration $f(n,t)$ of solute clusters of a given size n varying over the range from solute dimers to large incoherent precipitates. We use the discrete Master equation approach, i.e. the set of kinetic equations defined by the rates at which precipitates absorb a solute atom and lose a solute atom due to thermal evaporation and cascade destruction

$$\frac{\partial f(2,t)}{\partial t} = 2W^+(1)C_A - (W^+(2) + W^-(2))f(2,t) + W^-(3)f(3,t), \tag{9}$$

$$\frac{\partial f(n,t)}{\partial t} = J_{n-1,n} - J_{n,n+1}, \quad n \geqslant 3, \tag{10}$$

$$J_{n-1,n} = W^+(n-1)f(n-1,t) - W^-(n)f(n,t). \tag{11}$$

Using Eq. (8) we construct the absorption and emission rates of solute monomers. Probabilities to absorb/emit a solute atom by precipitates include the coherent and incoherent contributions; the probability to emit a solute atom contains also the term responsible for cascade dissolution

$$W^+(n) = W^+_{coh}(n)p(n) + W^+_{inc}(n)(1 - p(n)), \tag{12}$$

$$W^-(n) = W^-_{coh}(n)p(n) + W^-_{inc}(n)(1 - p(n)) + \frac{4\pi R(n)}{\omega}D_{mix}, \tag{13}$$

$W^+_{\alpha}(n)$ and $W^-_{\alpha}(n)$ are the absorption and emission rates for coherent and incoherent precipitates

$$W^+_{\alpha}(n) = \frac{4\pi}{\omega}R(n)D_A^{\alpha}C_A, \tag{14}$$

$$W^-_{\alpha}(n) = \frac{4\pi}{\omega}R(n)D_A^{\alpha}C_A^{R,\alpha}, \quad \alpha = coh, inc. \tag{15}$$

The first term in Eq. (9) for dimers takes into account that the relative diffusivity of the monomer pair is twice as much as the monomer diffusivity.

Here we do not consider the populations of coherent and incoherent precipitates separately. Instead we introduce different probabilities to absorb solute atoms by coherent and incoherent precipitate. The advantage of this approach is that we can include in the model the population of semicoherent precipitates (at least qualitatively). As can be seen from Eqs. (12) and (13), $p(n)$ has the

meaning of the probability for a precipitate to be coherent with the matrix.

We do not consider irradiation with A or B ions; therefore the total number of mobile monomers and solute atoms in all clusters is conserved in the system

$$C_A + \sum_{n=2}^{\infty} n f(n,t) = Q, \tag{16}$$

where Q is the volume fraction of solute atoms. Below we will use this mass-balance condition in a differential form

$$\frac{dC_A}{dt} = -\sum_{n=2}^{\infty} n \frac{\partial f(n,t)}{\partial t}. \tag{17}$$

Solute mobility depends on vacancy concentration which is determined from the quasi-stationary equation

$$K - \alpha_R D_i C_i C_V - k^2 D_V (C_V - C_V^e) = 0, \tag{18}$$

where D_i is the diffusion coefficient of interstitial atoms, C_i is the average concentration of interstitial atoms, α_R is the recombination rate constant and k^2 is the total sink strength. For the problem addressed here bias effects are not essential, therefore we use the usual relation

$$D_i C_i = D_V (C_V - C_V^e). \tag{19}$$

Then the vacancy supersaturation is given by

$$\frac{C_V}{C_V^e} = 1 + \frac{1}{2}\left(1 + \frac{k^2}{C_V^e \alpha_R}\right) \times \left\{ \sqrt{1 + \frac{4K}{\alpha_R D_V}\left(C_V^e + \frac{k^2}{\alpha_R}\right)^{-2}} - 1 \right\}. \tag{20}$$

The total sink strength contains contributions from semicoherent and incoherent precipitates which are sinks for PD

$$k^2 = k_0^2 + \frac{4\pi}{\omega} \sum_{n=n_{coh}}^{\infty} R(n) f(n,t)(1 - p(n)), \tag{21}$$

where k_0^2 is the 'background' sink strength of all other sinks except precipitates.

3. Numerical method

Because of non-linearity and complexity the set of kinetic equations formulated above can be solved only numerically. However, this problem is impossible to solve directly, even numerically, since the number of coupled equations amounts to the number of solute atoms in the largest precipitates present in the system, i.e. requirements to computer resources increase enormously with the precipitate size (for a system with precipitate sizes in the range of $R \leqslant 10$ nm the number of equations is more than 10^5). This difficulty is common in problems of the non-equilibrium evolution of cluster populations. Early efforts [26–35] in description of PD cluster nucleation and growth in metals under irradiation are reviewed in [36–39]. The general solution strategy of the hierarchy of rate equations for all cluster sizes is to reduce this discrete Master equation formulation to a continuous description and/or to a numerical scheme with a controlled number of equations.

Kiritani [29] has developed a method for analysis of the clustering process of supersaturated lattice vacancies, in which the first $N = 100$ equations are the rate equations describing only single cluster sizes, while above this number clusters within a range of sizes are grouped together with the same rate constants (the width of a group was less than or equal to five percent of the size of clusters in this group). Since the crossover value $N = 100$ is sufficiently large, it is likely that the grouping has little or no effect on the nucleation stage. The Master equation plus grouping approach has proved to be a useful approximate scheme. Hayns [31] has applied the Kiritani grouping scheme to study the nucleation and growth of interstitial loops during irradiation, and has shown that by making a suitable choice of group widths the discontinuities found by Koiwa [40] in the size distribution function can be minimized. Further development and improvement of the grouping method is described in [41,42].

The most well known traditional method to address the numerical difficulties of the discrete Master equation approach is a continuum approximation for the cluster sizes. The Master equation is transformed, by the Taylor series expansion up to the second-order terms, into the partial differential equation (PDE) of the Fokker–Planck type for the distribution with the continuous size variable. In general, the truncation of the Taylor series at the second derivative is invalid for small-sized clusters, i.e. in the size range where rate constants and distribution functions change fast. Therefore, a hybrid method has been developed by Ghoniem and Sharafat [37]. In this method to conserve the details of small-size clustering the separate rate equations are used for vacancy and interstitial clusters up to

$N = 4$; larger size defects are simulated by converting the set of rate equations into the Fokker–Planck equation. To solve numerically the Fokker–Planck equation for high irradiation doses (large cluster sizes) Ghoniem and Sharafat [37] introduce a new variable that is related to the cluster radius r by a logarithmic transformation $u = \ln(2r/b)$ (where b is the Burgers vector); then they divide the continuous domain into equal sized elements and discretize the transformed Fokker–Planck equation. Computational efficiency can be improved further using the atom conservation principle to determine dynamically the necessary number of equations solved simultaneously [35].

The hybrid method similar to that described in [37] has been applied recently by Ozkan and Ortoleva [43] to model nucleation, Ostwald ripening and stepping in the silica polymorph system. In this method the cluster size domain is divided into two parts; for small clusters ($n < N \sim 100$) discrete kinetic equations are applied, while for large clusters a continuous kinetic equation is written with respect to the $\ln(n)$ variable. In this approach the boundary condition between the discrete and continuous formulations are obtained from the continuity conditions [43].

In the methodology of Kampmann and Wagner [44,45] the kinetics of small-sized clusters is not considered; instead, the classical nucleation theory is used to derive the nucleation rate as a function of time and solute concentration. In order to simulate the precipitation kinetics the continuous time evolution is divided up into a discrete number of small time steps. At each step, new particles are allowed to nucleate and existing particles grow (or shrink). The radius of the newly formed particles is set to be slightly larger than the critical radius to enable these particles to grow. The size distribution of the particles is updated accordingly and used to calculate the volume fraction of particles and hence the instantaneous mean solute concentration in the matrix. The updated mean solute concentration is then used in calculating the nucleation and growth rates in the next time step. In this way, the overlap of nucleation, growth and coarsening during precipitation can be modeled [46].

Recently Surh et al. [47] have proposed a new combined method, based on the Master equation for small sizes and on a continuum Langevin Monte Carlo scheme to solve the Fokker–Planck equation for large sizes. The Master equation is used for small integer-sized voids up to $N = 2000$. During computational time step the clusters, which grow to this upper boundary, are removed. The loss is compensated by creating a new Langevin particle at position $n = N$ with weight equal to the density of clusters lost. A biased random-walk of Langevin particles approximates the Fokker–Planck evolution. The clusters in a given Langevin particle are constrained to stay together in size as they evolve, and the Langevin particle weight remains constant over time [47].

In our study, to reduce drastically the number of equations we propose a new realization of the hybrid (or combined) approach that is rather simple and straightforward methodologically as compared to methods discussed above. Similar to [37,43] we keep the original finite difference set of equations up to some number, $N \gg 1$, of atoms in clusters. For larger sizes, the discrete Master equation is transformed, by the Taylor series expansion up to the second-order terms, into the continuous Fokker–Planck equation

$$\frac{\partial f(x,t)}{\partial t} = \frac{\partial}{\partial x}\left(-A(x)f(x,t) + \frac{1}{2}\frac{\partial}{\partial x}B(x)f(x,t)\right), \quad x > N, \tag{22}$$

where $A(x)$ is the drift rate proportional to the growth rate (8)

$$A(x) = W^+(x) - W^-(x) = A_0(x) - \frac{4\pi R(x)}{\omega} D_{\mathrm{mix}} \tag{23}$$

and $B(x)$ describes diffusion in the size space

$$B(x) = W^+(x) + W^-(x) = B_0(x) + \frac{4\pi R(x)}{\omega} D_{\mathrm{mix}}, \tag{24}$$

where $A_0(x)$ and $B_0(x)$ correspond to the case without cascade effects ($D_{\mathrm{mix}} = 0$).

The combined set of equations – the discrete Master equation and the continuous Fokker–Planck equation – is solved numerically using a technique known as the method of lines (MOL) [48,49]. In the method of lines, the space and time discretizations of a PDE are decoupled and analyzed independently. First, the spatial derivatives are replaced with algebraic approximations over a spatial mesh, keeping the time derivatives continuous. The resulting system of initial-value ordinary differential equations (ODEs) is then integrated numerically using a suitable ODE integrator.

As it will be seen below, in our problem some kind of non-uniform mesh is highly desirable in

order to reduce the number of ODEs and, at the same time, to allow adequate resolution of the rapidly changing distribution function (i) in the region of small cluster sizes, (ii) at a moving front and (iii) in the vicinity of the stable size. An adaptive mesh scheme, which automatically tracks the regions of sharp spatial variation, is probably the most efficient option to do this (see, for example [50]). However, for present purposes we have instead chosen a much simpler non-adaptive non-uniform mesh scheme, where the mesh spacing varies smoothly in a preset way across the computational domain. To create the non-uniform mesh we use the following relations for mesh points x_i and mesh spacings Δx_i

$$\begin{aligned} &x_1 = 1, \\ &x_i = x_{i-1} + \Delta x_i, \quad 2 \leqslant i \leqslant M, \\ &\Delta x_i = \begin{cases} 1, & \text{for } 2 \leqslant i \leqslant N, \\ \Delta x_{i-1} \exp(\varepsilon), & \text{for } N < i \leqslant M, \end{cases} \end{aligned} \tag{25}$$

where M is sufficiently large so that the boundary condition $f(x_M) = 0$ is fulfilled. The variation of mesh spacing is controlled by the parameter ε that should be small, $|\varepsilon| \ll 1$. For positive ε the spacing between mesh points increases exponentially with point number i, therefore the number of equations can be reduced substantially due to coarse-graining of the numerical mesh. The increasing mesh spacing is especially useful, for example, in the Ostwald ripening problem, when the cluster mean size and the width of the size distribution increase with time. For constant and positive ε it is easy to find from Eq. (25) the explicit relation between mesh point x_i and point number i

$$\begin{aligned} &i = N + \frac{1}{\varepsilon} \ln\left(1 + \frac{\exp(\varepsilon) - 1}{\exp(\varepsilon)}(x_i - N)\right), \quad x \geqslant N, \\ &\varepsilon = \text{const} > 0. \end{aligned} \tag{26}$$

Asymptotically, at $i \gg N$ and $\varepsilon x_i \gg 1$, we obtain from (26)

$$i = \frac{1}{\varepsilon} \ln(\varepsilon x_i). \tag{27}$$

This relation is of the same nature as the logarithmic transformation $u \sim \ln(x)$ used in [37,43].

Mesh definition (25) allows one to change the spacing between mesh points in a more sophisticated way. That is, introducing a non-monotonic dependence of ε on mesh point number i, we can adjust the mesh to the expected behavior of the solution in special size regions after a test run of the algorithm (see the next section).

The PDE (22) is transformed to conservative finite difference equations on the non-uniform mesh (25). The right hand side of the PDE containing the size variable is discretized using central finite differencing. As a result we obtain the set of ODEs in t approximating the PDE

$$\begin{aligned} \frac{\mathrm{d}f_i}{\mathrm{d}t} = \frac{1}{\Delta x_{i+1} + \Delta x_i} \Bigg[&-(A_{i+1} f_{i+1} - A_{i-1} f_{i-1}) \\ &+ \left(\frac{B_{i+1} f_{i+1} - B_i f_i}{\Delta x_{i+1}} - \frac{B_i f_i - B_{i-1} f_{i-1}}{\Delta x_i} \right) \Bigg]. \end{aligned} \tag{28}$$

Here and below the subscript i refers to function values in mesh points, $f_i = f(x_i, t)$, etc. The remarkable property of Eq. (28) is that on the mesh with equidistant points ($\Delta x_i = 1$) it reduces to the initial discrete Master equation (10). Therefore Eq. (28) can be used in the whole domain of cluster sizes $n \geqslant 3$, i.e. the transition from the discrete Master equation ($x_i \leqslant N$) to the finite difference PDE ($x_i > N$) is seamless. In other words, in our numerical approach to ensure matching between the rate theory solution and the Fokker–Planck solution, we need no special modifications to the first continuum equation or the boundary condition between the discrete and continuous formulations, as distinct from numerical methods of Refs. [37,43], respectively.

The summation in Eqs. (17) and (21) is replaced by the numerical integration using the trapezoidal rule for unequally spaced abscissas

$$\frac{\mathrm{d}C_\mathrm{A}}{\mathrm{d}t} = -\sum_{i=2}^{M} x_i \frac{\mathrm{d}f_i}{\mathrm{d}t} \Delta z_i, \tag{29}$$

$$k^2 = k_0^2 + \frac{4\pi}{\omega} \sum_{i=n_\mathrm{coh}}^{M} R_i (1 - p_i) f_i \Delta z_i, \tag{30}$$

where $\Delta z_i = 0.5(\Delta x_i + \Delta x_{i+1})$.

The initial value problem for the set of ODEs (28) and (29) can be solved by a standard numerical package for stiff ODE sets. Stiffness is the generic feature of this type of evolution equations; it is related to the fact that the population of small solute clusters and the vacancy concentration adjust very fast to slow changes in the system parameters which are controlled by large clusters and precipitates. We use the RADAU code that has been developed for stiff and differential-algebraic problems [51]. This code is based on the implicit Runge–Kutta method of variable order with an adaptive time-step control. The stability properties and the high order

make this method suitable for large sets of stiff ODEs.

Several remarks should be made about the choice of the Master equation cutoff N. As will be seen from the simulation results presented below the quasi-stationary distribution of solute clusters forms rapidly in the region of small sizes. This distribution, as a function of cluster size, decreases steeply from the dimer concentration to values of several orders of magnitude smaller. There exists a gap in the solute cluster distribution, separating the population of small clusters from the distribution of large precipitates. Following Frenkel [52,53] we call the distribution of small-sized clusters, which nucleate and decay continuously, the heterophase fluctuations [24,54]. The size width of the region of heterophase fluctuations depends on material parameters and temperature. In particular, it increases with decreasing the interphase energy [54]; and this effect is especially pronounced in case of coherent precipitates that possess low interphase energy. This means that heterophase fluctuations may contribute considerably to the overall balance of solute atoms and influence the kinetics of large precipitates. Obviously, to describe adequately the nucleation stage and the kinetics of heterophase fluctuations the Master equation cutoff N should be chosen to lie outside the region of heterophase fluctuations. Exactly in the region of heterophase fluctuations the Taylor series expansion of the distribution function is not valid; hence, we use the discrete Master equation (see Eqs. (9)–(11)) or equivalent Eq. (28) with $\Delta x_i = 1$. Since the kinetics of heterophase fluctuations is fast, the optimum value of N (the number of equidistant mesh points, $\Delta x_i = 1$, $i \leqslant N$) can be estimated from a short simulation of a low dose irradiation, using a large guess value of N.

4. Simulation results

Material parameters used in simulations are listed in Table 1. For simplicity, energies of coherent interfaces and incoherent ones are assumed to be the same. This set of parameters is basically the same as that used in our paper for model calculations of the radiation-modified phase diagram of Zr–Nb alloy [24]. Irradiation conditions and the solute content are so chosen that coherent precipitates are stable whereas incoherent ones are unstable (see Fig. 1). Therefore we expect that in this region the population of semicoherent precipitates may form after prolonged irradiation. To illustrate the point Fig. 2 shows the precipitate growth rate, Eq. (8), as a function of precipitate radius. It is seen that small precipitates cannot grow to sizes larger than the stable size, while large incoherent precipitates should shrink to the stable size.

Table 1
Material parameters used in calculations

Parameter	Value
Temperature, K	600
Geeration rate of freely migrating point defects, K, dpa/s	10^{-7}
Cascade mixing efficiency, d_{mix}, nm^2	4
Atomic volume, ω, m^{-3}	2.4×10^{-29}
Recombination rate constant, α_{R}, m^{-2}	3×10^{20}
Initial strength of sinks, k_0^2, m^{-2}	5×10^{14}
Equilibrium vacancy concentration, $C_{\mathrm{V}}^{\mathrm{e}}$, at. fraction	$0.54\exp(-1.8\ \mathrm{eV}/k_{\mathrm{B}}T)$
Diffusion coefficient of vacancies, D_{V}, m^2/s	$1.67\times10^{-4}\exp(-1.37\ \mathrm{eV}/k_{\mathrm{B}}T)$
Equilibrium concentration of monomers, $C_{\mathrm{A}}^{\mathrm{e}}$, at.%	0.5
Total solute content, Q, at.%	2.5
Interphase energy, γ, J/m^2	0.1
Coherency loss parameter (see Eq. (7)), n_{coh}	75
Coherency loss parameter (see Eq. (7)), $R_{\mathrm{loss}} = \sqrt[3]{3n_{\mathrm{loss}}\omega/4\pi}$, nm	7
Width of the coherency loss region (see Eq. (7)), Δn	10^4

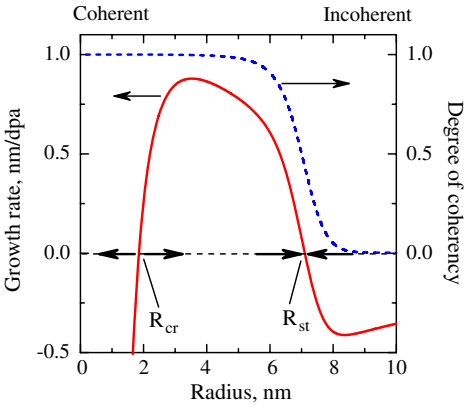

Fig. 2. The growth rate (solid line) and the degree of coherency (dashed line, Eq. (7)) versus precipitate radius. The growth rate of incoherent precipitates is negative. The concentration of solute monomers $C_{\mathrm{A}} = 0.8$ at.%. R_{cr} and R_{st} are critical and stable radii, respectively.

4.1. Solution-annealed alloy

Let us consider homogeneous nucleation of precipitates and evolution of their size distribution in a solution-annealed alloy under cascade-producing irradiation. In the initial state the matrix contains only solute monomers with the concentration $C_A = Q = 2.5$ at.%. The initial value problem for the ODE set given by Eq. (28) has been solved in the size region from dimers to precipitates containing 8.5×10^4 solute atoms (radius of about 7.8 nm). The mesh defined by Eq. (25) with increasing mesh spacing ($N = 50$ and $\varepsilon = 5 \times 10^{-3}$) was used up to the cluster radius $0.7R_{\text{loss}}$ ($\Delta x = 105.11$). For cluster sizes $R > 0.7R_{\text{loss}}$, the decreasing mesh spacing with $\varepsilon = -10^{-3}$ was used, because in this size region the formation of a narrow distribution function was expected. The chosen mesh allowed us to reduce the total number of ODE solved simultaneously to 1923.

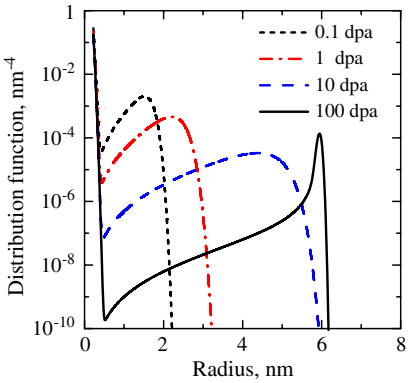

Fig. 3. The simulated distribution function of solute clusters which formed in the solid solution during irradiation up to 100 dpa. Dose is defined as Kt.

Fig. 3 shows the distribution function of solute clusters defined in terms of cluster radius

$$F(R,t) = \frac{3}{\omega}\left(\frac{4\pi}{3\omega}\right)^{1/3} n^{2/3} f(n,t). \tag{31}$$

It is seen that the nucleation stage has been completed very fast and after a short transient period the quasi-stationary distribution of small clusters ($R < 1$ nm) has formed. The leading edge of the distribution advances with time, but it cannot move into the region of incoherent precipitates where the drift rate $A(x)$ is negative. As a result the narrow distribution of semicoherent precipitates forms at a radius of about 6 nm.

To analyze the simulation results we divide the population of precipitates into two groups: (i) small clusters (heterophase fluctuations) which contain less than $n^* = 75$ atoms ($R < R^* = 0.75$ nm); and (ii) large precipitates. Fig. 4(a) shows the dose dependence of the heterophase fluctuation density N_{hf} and the precipitate density N_{p}

$$N_{\text{hf}} = \frac{1}{\omega}\sum_{i=2}^{i^*} f(x_i,t)\Delta z_i \approx \int_{R_2}^{R^*} F(R,t)\,\mathrm{d}R, \tag{32}$$

$$N_{\text{p}} = \frac{1}{\omega}\sum_{i=i^*}^{M} f(x_i,t)\Delta z_i \approx \int_{R^*}^{\infty} F(R,t)\,\mathrm{d}R, \tag{33}$$

where i^* is the index number of the mesh point $x_{i^*} = n^*$ and R_2 is the dimer radius.

After 0.1 dpa the density of heterophase fluctuations remains almost constant up to 100 dpa, while

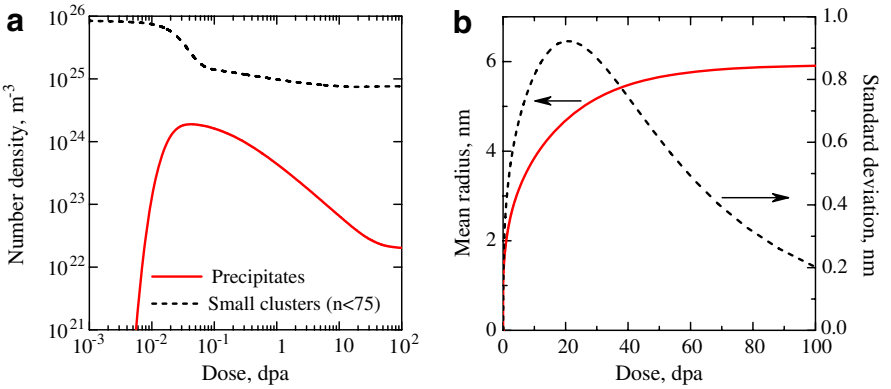

Fig. 4. Dose dependence of the mean parameters of solute clusters in solid solution under irradiation: (a) number densities of precipitates (solid line) and heterophase fluctuations (dashed line); (b) the mean radius of precipitates (solid line) and the standard deviation (dashed line) of the precipitate distribution.

the population of large precipitates undergoes a process akin to the Ostwald ripening, i.e. the number density of precipitates decreases (Fig. 4(a)). At about 40 dpa the alloy reaches the slowly-evolving state: both the number density and the mean radius of precipitates tend to steady state values (Fig. 4). The mean radius of precipitates is defined as

$$R_{\mathrm{mean}} = \frac{1}{\omega N_{\mathrm{p}}} \sum_{i=i^*}^{M} f(x_i,t) R(x_i) \Delta z_i \approx \frac{1}{N_{\mathrm{p}}} \int_{R^*}^{\infty} F(R,t) R \, \mathrm{d}R. \quad (34)$$

Fig. 4(b) shows also the dose dependence of the standard deviation σ

$$\sigma^2 = \frac{1}{\omega N_{\mathrm{p}}} \sum_{i=i^*}^{M} f(x_i,t)[R(x_i) - R_{\mathrm{mean}}]^2 \Delta z_i \approx \frac{1}{N_{\mathrm{p}}} \int_{R^*}^{\infty} F(R,t)(R - R_{\mathrm{mean}})^2 \, \mathrm{d}R, \quad (35)$$

which is related to the width of the precipitate distribution. It is seen that the distribution is getting narrow without any sign of saturation at 100 dpa.

Volume fractions of precipitates, heterophase fluctuations and solute monomers after 10 dpa practically do not change (Fig. 5). For the material parameters used here, after the ending of the nucleation stage the volume fraction of heterophase fluctuations is small, it amounts to 0.04 at.%. In the final state the solid solution remains supersaturated, i.e. the concentration of solute monomers $C_{\mathrm{A}} = 1.4 C_{\mathrm{A}}^{\mathrm{e}} = 0.7$ at.%.

We have found that with decreasing the cluster interphase energy the volume fraction of hetero-

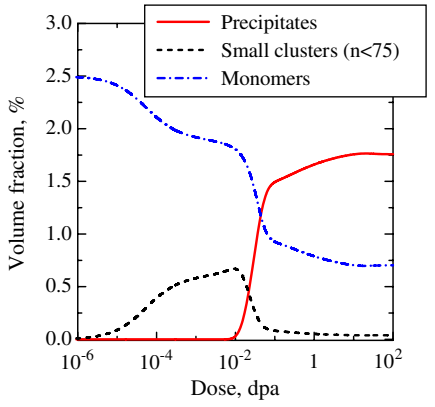

Fig. 5. Volume fractions of precipitates, heterophase fluctuations (small clusters, $n < 75$) and solute monomers versus irradiation dose.

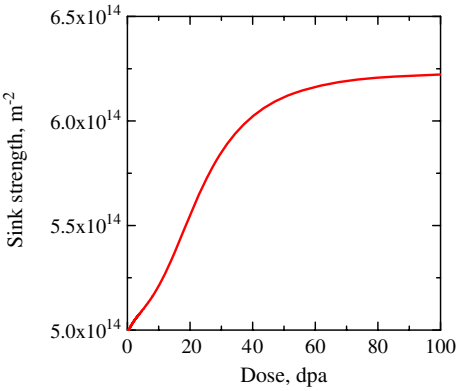

Fig. 6. Dose dependence of the total sink strength in irradiated solid solution.

phase fluctuations increases, whereas the rate of solid solution decomposition decreases. The reason is that in our model material at $T = 600$ K the main driving force for solute redistribution between coherent clusters is the thermal emission of solute atoms, which is controlled by the interphase energy (see Eq. (3)). At smaller values of interphase energy the small clusters are more stable thermally and their volume fraction is higher.

The total sink strength increases with dose because of growth of semicoherent precipitates which are sinks for PD (Fig. 6).

4.2. Aged alloy

In this section we simulate the cascade-induced shrinkage of thermally stable incoherent precipitates existing in the alloy prior to irradiation. In the initial state the alloy is supersaturated, $C_{\mathrm{A}} = 1.25 C_{\mathrm{A}}^{\mathrm{e}}$, and contains incoherent precipitates with the mean radius $R_0 = 11$ nm and the number density $N_0 = 3 \times 10^{21}$ m^{-3}. The total solute content is $Q = 2.5$ at.%. The initial size distribution was taken in the form of the Lifshitz–Slyozov distribution [55,56], which is observed normally in thermally aged alloys

$$F_0(R) = \frac{N_0}{R_0} g\left(\frac{R}{R_0}\right),$$

$$g(u) = \frac{4}{9} u^2 \left(\frac{3}{3+u}\right)^{7/3} \left(\frac{1.5}{1.5-u}\right)^{11/3} \times \exp\left(-\frac{u}{1.5-u}\right). \quad (36)$$

Fig. 7 shows the simulated distribution function along with the mesh used in calculations. Because of cascade-induced dissolution of incoherent precipitates

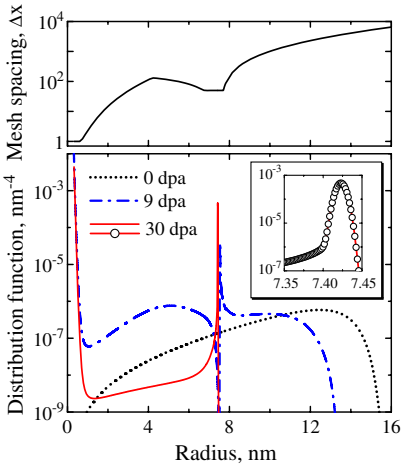

Fig. 7. The simulated evolution of the distribution functions of precipitates and solute clusters in the aged alloy during irradiation up to 30 dpa. In the upper part of the figure the calculation mesh is shown (note the logarithmic scale along the y-axis). Increasing mesh spacing ($\varepsilon = 0.01$) was used for cluster radii $R < 0.6R_{\text{loss}}$ and $R > 1.1R_{\text{loss}}$. The fine mesh with equidistant points was used in the vicinity of the stable radius in order to resolve the size distribution peak that is shown in the insert.

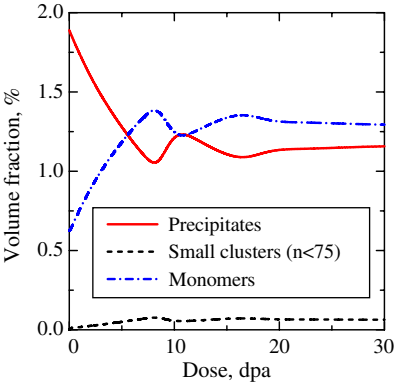

Fig. 8. Volume fractions of precipitates, heterophase fluctuations and solute monomers versus irradiation dose. Initial state corresponds to the aged alloy.

the size distribution shifts to smaller sizes. At the same time the monomer concentration increases well above the equilibrium concentration of monomers (Fig. 8) giving rise to nucleation and growth of coherent precipitates. As a result the bimodal distribution function forms. Ultimately, the precipitate population evolves to a very narrow distribution of semicoherent precipitates (Fig. 7). In the final state the volume fraction of mobile solute monomers is higher than the precipitate volume fraction.

Dose dependences of the number density and the mean radius of precipitates are shown in Fig. 9. At about 7 dpa the density of precipitates increases rapidly because of nucleation of small coherent precipitates. It is interesting that the second, more smooth, wave of renucleation is observed at about 15 dpa. The reason is that the homogeneous nucleation is an avalanche-like process which starts when a sufficiently high solute supersaturation is created in the material due to cascade dissolution of unstable precipitates. The sink strength and the standard deviation exhibit non-monotonic dose dependence because of dissolution of large precipitates and renucleation of small precipitates (Fig. 9).

Here, the Lifshitz–Slyozov initial distribution of precipitates was taken for the simulation. As we have checked, for similar initial mean radii and number densities the final parameters of precipitate distribution are insensitive to changes of the shape of the initial precipitate distribution.

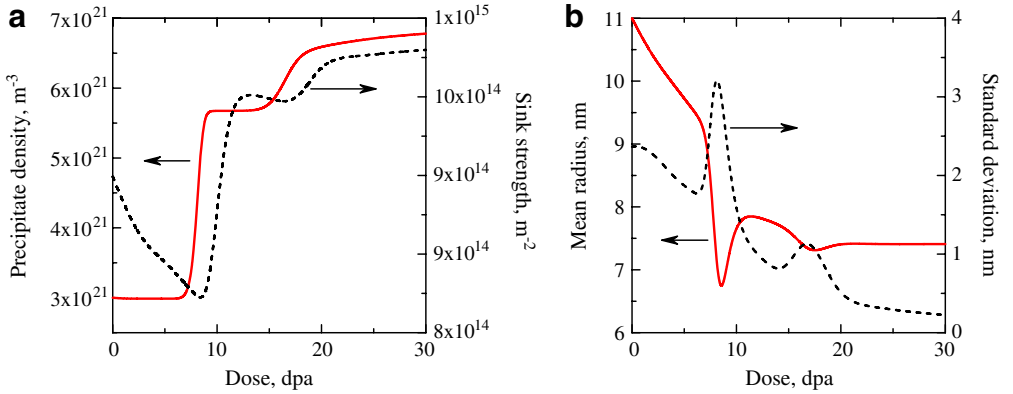

Fig. 9. Evolution of the mean parameters of solute clusters in aged alloy under irradiation. (a) The number density of precipitates (solid line) and the total sink strength (dashed line). (b) The mean radius of precipitates (solid line) and the standard deviation (dashed line). The standard deviation increases when new clusters nucleate.

5. Discussion

Our main goals were (i) to show the important consequences of coherency loss and (ii) to demonstrate the numerical method to solve kinetic equations of evolution of the cluster population from the early nucleation stage to the later asymptotic or quasi-stationary stage.

We describe the coherency loss in a phenomenological way, using two parameters: the size of transformation into the incoherent state and the width of transformation region in the size space. More detailed description is not possible at present. Nevertheless our approach turned out to be useful for prediction of possible paths of non-equilibrium evolution of complicated systems such as alloys under irradiation. Numerical results presented above show that both in the solution-annealed alloy and in the aged one the narrow slowly-evolving distributions of semicoherent precipitates form under irradiation. However, quasi-stationary states in these two alloys differ, i.e. precipitate mean radii and number densities differ. At first glance, the final asymptotic state should not depend on initial state of the alloy. To explain this dependence let us consider Fig. 10. It is seen that all precipitates have accumulated in the point of stable size where the growth rate is zero. In the case of solid solution critical and stable radii are close to each other; in the case of aged alloy these two radii differ considerably.

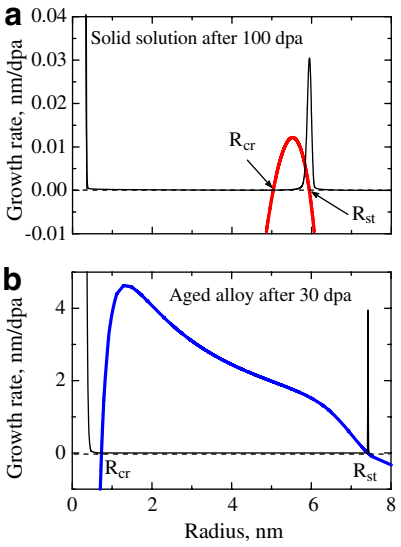

Fig. 10. Size dependence of precipitate growth rate (thick solid line) and precipitate distribution functions (thin solid lines) formed in the solution-annealed alloy (a) and in the aged alloy (b). Irradiation dose of the solution-annealed alloy is 100 dpa. Irradiation dose of the aged alloy is 30 dpa. Distribution functions are normalized to arbitrary values.

The critical and stable radii, R_{cr} and R_{st}, approach each other if the concentration of solute monomers decreases due to precipitate growth and/or nucleation of small clusters. In the case of aged alloy, initially, cascades dissolve large precipitates; this results in increase of the solute supersaturation. At a sufficiently high supersaturation at about 7 dpa the nucleation process is triggered; and after 2 dpa the nucleation rate drops down drastically (Fig. 9(a)), despite the fact that the solution remains supersaturated (Fig. 8). At the same time, the newly-nucleated, growing clusters ($R_{cr} < R < R_{st}$) absorb only a small fraction of solute monomers. This means that the supersaturation does not decrease substantially during evolution, i.e. R_{cr} and R_{st} remain separated even after the second wave of nucleation observed after 15 dpa (Fig. 9(a)). Thus, because of a strong dependence of the nucleation rate on solute supersaturation, the asymptotic behavior of the irradiated alloy depends on alloy initial state – whether simulation started from the solid solution or from the aged alloy. In other words, depending on the degree of competition between nucleation, precipitate growth and cascade dissolution, the system becomes arrested in different kinds of quasi-stationary asymptotic states. From a practical point of view, by preparing a certain initial state of the alloy one can select the proper quasi-stationary asymptotic state and the time to reach this state.

To check the argumentation presented above we have simulated the alloy evolution for a higher nucleation rate, i.e. for a smaller value of the interphase energy, $\gamma = 5 \times 10^{-2}$ J/m^2. Fig. 11 shows that in this case the asymptotic state of the alloy does not depend on initial state of the alloy.

Since in the stable point, where all precipitates accumulate, the drift rate $A(x)$ is zero (see Eq. (22)), at a later stage of evolution the diffusion in the size space determines the width of the size distribution and the time to reach quasi-steady state. We used above the simplified model of cascade dissolution. It was assumed that due to cascade impacts the solute atoms are ejected from the precipitate one by one, similar to thermal evaporation. In reality, a cascade can remove at a time several solute atoms from the precipitate, or even can disperse the small precipitate/cluster completely [57], i.e. the number

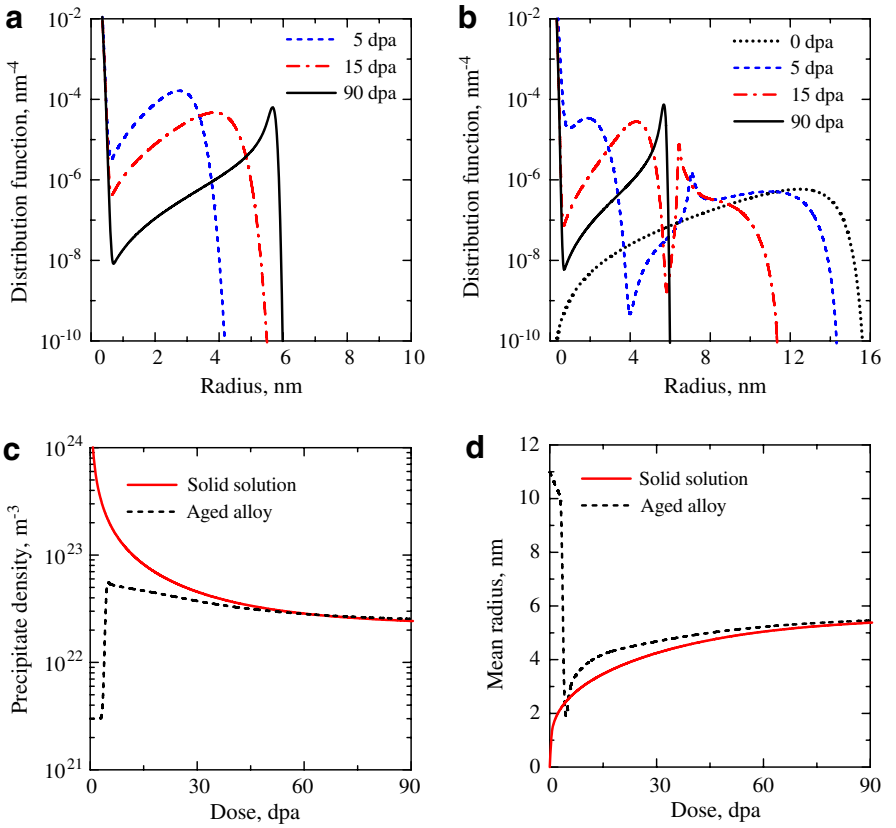

Fig. 11. Evolution of precipitate population in the case of relatively small interphase energy, $\gamma = 5 \times 10^{-2}$ J/m^2. The simulated evolution of the distribution functions of precipitates and solute clusters in the solid solution (a) and in the aged alloy (b). The final values of the precipitate number density (c) and the mean radius (d) does not depend on initial state of the alloy.

of atoms removed by cascades from the precipitate undergoes large fluctuations. Let us discuss schematically the influence of this effect on evolution of the precipitate size distribution. In order to take into account the stochastic nature of cascade-induced dissolution, Eqs. (10) and (11) for large precipitates should be rewritten in the form

$$\frac{\partial f(n,t)}{\partial t} = J^0_{n-1,n} - J^0_{n,n+1} - f(n,t)\sum_{k=1}^{k_m} W_C(k,n) + \sum_{k=1}^{k_m} W_C(k,n+k) f(n+k,t), \tag{37}$$

where $J^0_{n-1,n}$ is the cluster flux in the size space without cascade effects, i.e. $J^0_{n-1,n}$ is given by Eqs. (11)–(13) in which D_{mix} is set to zero. Other terms correspond to cascade dissolution: $W_C(k,n)$ is proportional to the probability for a cascade to remove k solute atoms from the precipitate containing n solute atoms and k_m is the maximum number of solute atoms which can be removed from the precipitate by a cascade. For large precipitates ($n \gg k_m$), Eq. (37) is transformed by the Taylor series expansion into the Fokker–Planck equation similar to Eq. (22), but with different drift rate and diffusion coefficient

$$A(x) = A_0(x) - \sum_{k=1}^{k_m} k W_C(k,n), \tag{38}$$

$$B(x) = B_0(x) + \sum_{k=1}^{k_m} k^2 W_C(k,n). \tag{39}$$

In order to describe correctly dissolution of large precipitates the drift rate, Eq. (38), should be approximately the same as that given by Eq. (23), i.e.

$$\sum_{k=1}^{k_m} k W_C(k,n) \cong \frac{4\pi R(n)}{\omega} D_{\mathrm{mix}}. \tag{40}$$

As regards the cascade contribution to the diffusion coefficient in the size space, it can be estimated as follows:

$$\sum_{k=1}^{k_m} k^2 W_C(k,n) \geqslant \left(\sum_{k=1}^{k_m} W_C(k,n)\right)^{-1} \left(\sum_{k=1}^{k_m} kW_C(k,n)\right)^2 = \bar{k}\frac{4\pi R(n)}{\omega} D_{\mathrm{mix}}, \tag{41}$$

where

$$\bar{k} = \left(\sum_{k=1}^{k_m} W_C(k,n)\right)^{-1} \sum_{k=1}^{k_m} kW_C(k,n) \tag{42}$$

is the mean number of solute atoms removed by one cascade from the precipitate. According to Eq. (41), the cascade contribution to the diffusion coefficient $B(x)$ is at least $\bar{k}$ times larger than in the model simulated in this paper. This means that the width of the precipitate distribution in the final state should be larger. Indeed, in the quasi-stationary state all precipitates accumulate in the vicinity of the stable size x_{st}, where the drift rate can be approximated by a linear function of size

$$A(x) = -a(x - x_{\mathrm{st}}), \quad a = \left|\frac{\mathrm{d}A(x_{\mathrm{st}})}{\mathrm{d}x_{\mathrm{st}}}\right|. \tag{43}$$

The steady state solution to the Fokker–Planck equation in the vicinity of the stable point is the Gaussian distribution

$$f(x) = N_{\mathrm{p}}\omega \frac{1}{\sigma\sqrt{2\pi}} \exp\left(-\frac{(x - x_{\mathrm{st}})^2}{2\sigma^2}\right), \tag{44}$$

where σ is the standard deviation of the distribution (which is about the half width at half maximum)

$$\sigma = \sqrt{\frac{B(x_{\mathrm{st}})}{2a}}. \tag{45}$$

Since in the stable point $C_{\mathrm{A}}^{\mathrm{R}} \approx C_{\mathrm{A}}^{\mathrm{e}}$, we obtain

$$B(x_{\mathrm{st}}) = \frac{4\pi R_{\mathrm{st}}}{\omega} D_{\mathrm{mix}} \frac{2 + (\bar{k}+1)\Delta}{\Delta}, \tag{46}$$

where $\Delta = (C_{\mathrm{A}} - C_{\mathrm{A}}^{\mathrm{e}})/C_{\mathrm{A}}^{\mathrm{e}}$ is the supersaturation. According to Eq. (46), the width of the precipitate size distribution increases, when we take into account large fluctuations in dissolution events due to cascades. The corresponding factor is given by

$$\frac{\sigma_{\bar{k}}}{\sigma_1} = \sqrt{\frac{2 + (\bar{k}+1)\Delta}{2(1+\Delta)}} < \sqrt{\frac{\bar{k}+1}{2}}. \tag{47}$$

Assuming that $\bar{k} = 100$, for the aged alloy simulated in Section 4.2 we find that the distribution remains rather narrow, $\sigma_{100} = 5.6\sigma_1 \approx 1.3$ nm.

The numerical method proposed in this paper proved to be very efficient for simulation of nucleation and evolution of second-phase particles. We also tested successfully our method on a problem of thermal decomposition of supersaturated solid solutions. It is known that during the later stage of decomposition (the Ostwald ripening), the precipitate size distribution exhibits scaling behavior as predicted by the Lifshits–Slezov theory of coarsening [55,56]. To assess accuracy and convergence of our numerical method the asymptotic solutions by Lifshits and Slezov have been compared with numerical results. We have found that during the later stage the precipitate size distribution, when scaled by the mean radius, tends towards a steady state shape, which closely matches the shape expected from the Lifshits–Slezov coarsening theory. The advantage of our approach is that using the same kinetic model and numerical method one can describe both the nucleation stage and the crossover to the final Ostwald ripening regime, as well as influence of initial conditions, heterophase fluctuations and diffusion in the size space on coarsening behavior of the precipitate population. We are going to address these questions in a separate publication.

6. Conclusions

1. The model has been formulated to describe evolution of the mixed population of coherent, semicoherent and incoherent precipitates.
2. The new numerical implementation of the hybrid approach has been proposed for simulation of nucleation and growth kinetics of cluster populations. In our method the hybrid approach is combined with the flexible meshing scheme that has the following advantages:
   - the spacing between mesh points can be adjusted to peculiarities of the solution behavior;
   - the crossover from discrete to continuous formulations can be chosen at any cluster size, depending on problem;
   - the discretized Fokker–Planck equation can be used for cluster sizes $n \geqslant 3$, i.e. matching of discrete and continuous solution is achieved automatically.
3. Coherency loss dramatically affects the development of precipitate population under cascade-producing irradiation. In a supersaturated alloy the transformation of precipitates to a less coherent structure decreases the rate of recovery due to

diffusion, i.e. the cascade-induced dissolution of semicoherent and incoherent precipitates is more efficient. At temperatures which can be determined from the radiation-modified diagrams, the competition between (i) nucleation and growth of coherent precipitates, (ii) coherency loss and (iii) cascade-induced dissolution of incoherent precipitates leads to formation of the narrow slowly-evolving size distribution of semicoherent precipitates.

4. The quasi-steady state of the precipitate population, which forms in the alloy after prolonged irradiation, may depend on initial state of the alloy.
5. The model of this paper can explain experimental observations such as (i) the lack of coarsening and decrease in size of Cu precipitates in Fe–Cu alloys irradiated with neutrons and ions at low temperatures and (ii) the absence of large incoherent precipitates in Zr–Nb alloys under reactor irradiation.

Acknowledgements

We would like to thank Yu.A. Turkin (Max-Planck-Institute for Plasma Physics) for helpful discussions of computational aspects of the problem.

References

[1] J.A. Hudson, D.J. Mazey, R.S. Nelson, in: S.E. Pugh, M.N. Loretto, D.I.R. Norris (Eds.), Voids Formed by Irradiation of Reactor Materials, BNES, London, 1971, p. 215.
[2] A.M. Parshin, Structure Strength and Radiation Damage of Corrosion-Resistant Steels and Alloys, Metallurgy Publ, Chelyabinsk, 1988 (in Russian).
[3] V.V. Bryk, V.N. Voyevodin, V.F. Zelensky, I.M. Neklyudov, A.M. Parshin, in: N.M. Packan, R.E. Stoller, A.S. Kumar (Eds.), Effects of Radiation on Materials: 14th International Symposium, ASTM STP 1046, vol. I, American Society for Testing and Materials, Philadelphia, PA, 1989, p. 437.
[4] G.R. Odette, B.D. Wirth, D.J. Bacon, N.M. Ghoneim, MRS Bull. 26 (2001) 176.
[5] G.R. Odette, G.E. Lucas, Radiat. Eff. Def. Solids 144 (1998) 189.
[6] P.J. Othen, M.L. Jenkins, G.D.W. Smith, W.J. Phythian, Philos. Mag. Lett. 64 (1991) 383.
[7] R. Monzen, M. Iguchi, M.L. Jenkins, Philos. Mag. Lett 80 (2000) 137.
[8] H.A. Hardouin-Duparc, R.C. Doole, M.L. Jenkins, A. Barbu, Philos. Mag. Lett. 71 (1995) 325.
[9] A.C. Nicol, M.L. Jenkins, M.A. Kirk, in: S.J. Zinkle, G. Lucas, R. Ewing, J. Williams (Eds.), Proceedings of the International Symposium on the Microstructural Processes in Irradiated Materials, MRS Symposium Proceedings, vol. 540, Materials Research Society, Pittsburgh, PA, 1999, p. 409.
[10] J.T. Buswell, C.A. English, M.G. Hetherington, W.J. Pythian, G.D.W. Smith, G.M. Worral, in: N.M. Packan, R.E. Stoller, A.S. Kumar (Eds.), Effects of Radiation on Materials: 14th International Symposium, ASTM STP 1046, vol. II, American Society for Testing and Materials, Philadelphia, PA, 1990, p. 127.
[11] M.K. Miller, B.D. Wirth, G.R. Odette, Mater. Sci. Eng. A 353 (2003) 133.
[12] A.C. Nicol, M.L. Jenkins, N. Wanderka, C. Abromeit, in: S.J. Zinkle, G. Lucas, R. Ewing, J. Williams (Eds.), Proceedings of the International Symposium on the Microstructural Processes in Irradiated Materials, MRS Symposium Proceedings, vol. 540, Materials Research Society, Pittsburgh, Pennsylvania, 1999, p. 457.
[13] V.F. Urbanic, M. Griffiths, in: D.S. Gelles, R.K. Nanstad, A.S. Kumar, E.A. Little (Eds.), Effects of Radiation on Materials: 17th International Symposium, ASTM STP 1270, vol. I, American Society for Testing and Materials, Philadelphia, PA, 1996, p. 1088.
[14] O.T. Woo, R.M. Hutcheon, C.E. Coleman, Mater. Res. Soc. Symp. Proc. 373 (1995) 189.
[15] C.D. Cann, C.B. So, R.C. Styles, C.E. Coleman, J. Nucl. Mater. 205 (1993) 267.
[16] M. Griffiths, J.F. Mecke, J.E. Winegar, in: E.R. Bradley, G.P. Sabol (Eds.), Zirconium in the Nuclear Industry: 11th International Symposium, ASTM STP 1295, American Society for Testing and Materials, Philadelphia, PA, 1996, p. 580.
[17] C.E. Coleman, R.W. Gilbert, C.J.C. Carpenter, G.C. Weatherly, in: Phase Stability During Irradiation, AIME, 1981, p. 567.
[18] V. Perovic, A. Perovic, G.C. Weatherly, L.M. Brown, G.R. Purdy, R.G. Fleck, R.A. Holt, J. Nucl. Mater. 205 (1993) 251.
[19] V.F. Zelenskii, A.I. Stukalov, I.M. Nekludov, V.M. Gritsina, L.S. Ozhigov, V.N. Voevodin, V.I. Savchenko, N.M. Roenko, V.K. Shamardin, G.P. Kobylyanskiy, Probl. At. Sci. Technol. Ser.: Radiat. Damage Phys. Radiat. Mater. Sci. 1 (64) (1996) 39 (in Russian).
[20] S.A. Averin, V.L. Panshenko, A.V. Kozlov, L.P. Sinelnikov, V.N. Shishov, A.V. Nikulina, in: G.P. Sabol, G.D. Moan (Eds.), Zirconium in the Nuclear Industry: 12th International Symposium, ASTM STP 1354, American Society for Testing and Materials, Philadelphia, PA, 2000, p. 105.
[21] A.S. Bakai, A.A. Turkin, in: R.E. Stoller, A.S. Kumar, D.S. Gelles (Eds.), Effects of Radiation on Materials: 15th International Symposium, ASTM STP 1125, vol. I, American Society for Testing and Materials, Philadelphia, PA, 1992, p. 709.
[22] A.A. Turkin, A.S. Bakai, A.V. Buts, Mater. Sci. Forum 97–99 (1992) 343.
[23] A.A. Turkin, C. Abromeit, V. Naundorf, J. Nucl. Mater. 233–237 (1996) 979.
[24] A.A. Turkin, A.V. Buts, A.S. Bakai, J. Nucl. Mater. 305 (2002) 134.
[25] K.C. Russell, Adv. Colloid Interf. Sci. 13 (1980) 205.
[26] L.M. Brown, A. Kelly, R.M. Mayer, Philos. Mag. 19 (1969) 721.
[27] J.L. Katz, H. Wiedersich, J. Chem. Phys. 55 (1971) 1414.

[28] B.O. Hall, D.I. Potter, in: J.A. Sprague, D. Kramer (Eds.), Effects of Radiation on Structural Materials: 9th International Symposium, ASTM-STP-683, American Society for Testing and Materials, Richland, WA, 1979.
[29] M. Kiritani, J. Phys. Soc. Jpn. 35 (1973) 95.
[30] M.R. Hayns, J. Nucl. Mater. 56 (1975) 267.
[31] M.R. Hayns, J. Nucl. Mater. 59 (1976) 175.
[32] A.I. Bondarenko, Yu.V. Konobeev, Phys. Status Solidi (a) 34 (1976) 195.
[33] W.G. Wolfer, L.K. Mansur, J.A. Sprague, in: M.L. Bleiberg, J.W. Bennet (Eds.), Radiation Effects in Breeder Reactor Structural Materials: Proceedings of the International Conference, Scottsdale, AZ, New York, Metall. Soc. AIME, 1977, p. 841.
[34] K.C. Russell, Acta Metall. 19 (1971) 753;
K.C. Russell, Acta Metall. 26 (1978) 1615.
[35] N.M. Ghoniem, D.D. Cho, Phys. Status Solidi (a) 54 (1979) 171.
[36] B.O. Hall, J. Nucl. Mater. 91 (1980) 63.
[37] N.M. Ghoniem, S. Sharafat, J. Nucl. Mater. 92 (1980) 121.
[38] N.M. Ghoniem, Phys. Rev. B 39 (1989) 11810.
[39] N.M. Ghoniem, J. Nucl. Mater. 179 (1991) 99.
[40] M. Koiwa, J. Phys. Soc. Jpn. 37 (1974) 1532.
[41] S.I. Golubov, A.M. Ovcharenko, A.V. Barashev, B.N. Singh, Philos. Mag. A 81 (2001) 643.
[42] A.M. Ovcharenko, S.I. Golubov, C.H. Woo, H. Huang, Comput. Phys. Commun. 152 (2003) 208.
[43] G. Ozkan, P. Ortoleva, J. Chem. Phys. 112 (2000) 10510.
[44] R. Kampmann, R. Wagner, in: P. Hassen, V. Gerold, R. Wagner, M.F. Ashby (Eds.), Decomposition of Alloys: The Early Stages, Pergamon, Oxford, 1984, p. 91.
[45] R. Wagner, R. Kampmann, in: R.W. Cahn, P. Haasen (Eds.), Materials Science and Technology, vol. 5, VCH, Weinheim, 1991, p. 213.
[46] J.D. Robson, Acta Mater. 52 (2004) 4669.
[47] M.P. Surh, J.B. Sturgeon, W.G. Wolfer, J. Nucl. Mater. 325 (2004) 44.
[48] O.A. Liscovets, Differen. Equat. 1 (1965) 1308.
[49] W.E. Schiesser, The Numerical Method of Lines: Integration of Partial Differential Equations, Academic Press, New York, 1991.
[50] A. Vande Wouwer, P. Saucez, W.E. Schiesser (Eds.), Adaptive Method of Lines, Chapman & Hall CRC, 2001.
[51] E. Hairer, G. Wanner, in: Stiff and Differential-Algebraic Problems, Springer Series in Comput. Mathematics, vol. 14, Springer-Verlag, 1991, second revised ed. 1996.
[52] J. Frenkel, J. Chem. Phys. 7 (1939) 538.
[53] Ya.I. Frenkel, Kinetic Theory of Liquids, Oxford University, Oxford, 1946.
[54] A.A. Turkin, A.S. Bakai, A.V. Buts, in: W.C. Johnson, J.M. Howe, B.E. Laughlin, W.A. Sofa (Eds.), Solid to Solid Phase Transformations, Minerals Metals and Materials Society, Pittsburgh, PA, 1994, p. 987.
[55] I.M. Lifshitz, V.V. Slyozov, ZhETF 35 (1958) 479 (in Russian) [Sov. Phys. JETP 8 (1959) 331].
[56] I.M. Lifshitz, V.V. Slyozov, J. Phys. Chem. Solids 19 (1961) 35.
[57] A.S. Bakai, A.V. Buts, A.A. Turkin, Fiz. Met. Metalloved. 79 (2) (1995) 5 (in Russian) [English translation in: Phys. Met. Metallogr. 79 (2) (1995)].